submitted to *Geophys. J. Int.*

Acoustic full waveform inversion for 2-D ambient noise source imaging

Arjun Datta[1], Bharath Shekar[2], Pushp L. Kumar[1]

[1]*Department of Earth and Climate Science, Indian Institute of Science Education and Research, Pune, India*

[2]*Department of Earth Sciences, Indian Institute of Technology Bombay, Mumbai, India*

Accepted date. Received date; in original form date

This is a non peer reviewed pre-print submitted to EarthArxiv. It is being considered for publication in Geophysical Journal International.

SUMMARY

We present a method for estimating seismic ambient noise sources, by acoustic full waveform inversion of interstation cross-correlations. The method is valid at local scales for laterally heterogeneous media, and ambient noise sources confined to the Earth's surface. Synthetic tests performed using an actual field array geometry, are used to illustrate three unique aspects of our work. First: the method is able to recover noise sources of arbitrary spatial distribution, both within and outside the receiver array, with high fidelity. This holds true for complex velocity models and does not require a good initial guess for inversion, thereby bridging a clear gap in the existing research literature. Second: we analyse the extent of biases in source inversion, that arise due to inaccurate velocity models. Our findings indicate that source inversion using simplified (e.g. homogeneous) velocity models may work reliably when lateral variations in velocity structure are limited to 5 or 10% in magnitude, but is vitiated by strong variations of 20% or higher. Finally, our technique is implemented without the adjoint method, which is usually inextricably linked to full waveform inversion. Inversions are performed using source kernels computed for each receiver pair, and this approach is computationally tractable for real-world problems with small aperture seismic arrays.

Key words: Seismic noise; seismic interferometry; waveform inversion; inverse theory

1 INTRODUCTION

The study of the ambient seismic field, or seismic ambient noise as it is popularly known, is now firmly entrenched in mainstream seismological research. Ambient seismic sources can shed light on such natural phenomena as ocean wave coupling with the seafloor (e.g. Juretzek & Hadziioannou 2016), sediment transport in rivers (Tsai et al. 2012), glacier hydrology and dynamics (e.g. Aso et al. 2017; Labedz et al. 2022), tropical cyclones (e.g. Retailleau & Gualtieri 2019) and underground hydrothermal activity (e.g. Cros et al. 2011). On the other hand, seismologists are widely interested in using ambient noise as a tool for studying Earth structure, typically by applying interferometric techniques to extract meaningful signals from noise recordings (e.g. Shapiro & Campillo 2004). Even in this case, source information is essential because the spatial distribution of noise sources effectively determines whether inter-station Green's functions can be accurately recovered from noise cross-correlations (Roux et al. 2005; Snieder 2004). There is ample evidence for biases in structure estimation, arising from realistic distributions of ambient noise sources on Earth (e.g. Kimman & Trampert 2010; Yao & van der Hilst 2009). If one chooses instead to leverage the power of full waveform inversion (FWI), the assumption of Green's function retrieval is dropped and both sources and structure must be simultaneously estimated (Sager et al. 2018b; Zhou et al. 2022). Thus, regardless of one's particular interest in seismic ambient noise, the ability to determine the strength and locations of the noise sources is of vital importance.

Traditional, computationally cheap methods for locating ambient sources include beamforming (e.g. Gal et al. 2015; Gerstoft & Tanimoto 2007), matched-field processing (e.g. Cros et al. 2011) and backprojection (e.g. Liu et al. 2016) as well as cross-correlation based imaging (e.g. Ermert et al. 2016; Tian & Ritzwoller 2015). The last few years have witnessed the emergence of FWI methods, which seek to match observed noise cross-correlations with theoretically modelled ones, incorporating their finite frequency sensitivity to spatially distributed sources (Fichtner et al.

2017; Tromp et al. 2010). This paper focusses on FWI to recover noise source distribution with the assumption of a known structure model (Datta et al. 2019; Ermert et al. 2017, 2021; Igel et al. 2021; Xu et al. 2019, 2020). These 'source inversion' techniques are useful in their own right, and essential components in the toolkit for the larger problem of full waveform noise cross-correlation tomography (e.g. Sager et al. 2020).

FWI, by definition, entails wave-equation based forward modelling. However, different approximations to the seismic wave equation (e.g. acoustic vs. elastic) or different assumptions about the medium of propagation, lead to a family of methods achieving varying degrees of modelling rigour. From analytical modelling in homogeneous or laterally homogeneous media (Datta et al. 2019; Xu et al. 2019, 2020) to numerical simulations in spherically symmetric (Igel et al. 2021) or full 3-D Earth models (Ermert et al. 2017, 2021) at global scales, a variety of methods have been proposed. In this study, we present an approach using acoustic modelling in 2-D media that incorporates laterally heterogeneous structure information. Xu et al. (2020) used classic surface wave analysis on ambient noise data (Bensen et al. 2007) to estimate a uniform phase velocity required for forward modelling. With our approach, one can go a step further by using the 2-D phase or group velocity maps obtained from ambient noise surface wave tomography (Shapiro 2019).

Independent of our choice of modelling scheme, another highlight of this study, achieved by building on the work of Datta et al. (2019), is the ability to localize sources outside the sensor array. Previous non-global studies have had limited success in this regard. Xu et al. (2019), for example, reported that both traveltime and waveform inversion are only able to estimate rough source directions, when sources are outside the array. Our method recovers external source shapes and sizes fairly accurately, given a moderate inter-sensor path density. This holds good even when the inversion is initialised with a uniform source model.

The two aforementioned features of our method lend themselves readily to a scrutiny of the source-structure trade-off in seismic interferometry (Fichtner 2014), which is not very well documented. Xu et al. (2019) reported the failure of source inversion in case of inaccurate structure models, but only for homogeneous halfspace models devoid of lateral variations. Other studies have argued that misfit functions defined using measurements of waveform energy ought not to be sensitive to lateral structural variations (Igel et al. 2021; Sager et al. 2018a). We work with a waveform energy misfit, only slightly different from that used in said studies, and find that structure (velocity) information does impact source inversion.

In the following, we first present the methodology for forward and inverse modelling (Section 2), followed by the synthetic tests (Section 3) which form the basis of our conclusions (Section 4).

2 CROSS-CORRELATION MODELLING AND INVERSION

Datta et al. (2019) introduced a method for estimating noise source directionality in a homogeneous medium. The limitation of estimating only directions was imposed by the choice of model parameterization, and the homogeneous medium assumption allowed for cross-correlations to be modelled analytically. In this study, we extend their method on both fronts. A similar but less restrictive model parameterization allows actual source locations and shapes to be estimated, and integration with a numerical solver eliminates the need to assume a homogeneous medium. However the choice of measurement, calculation of kernels and inversion strategy, remain essentially unchanged.

2.1 Forward modelling

The foundation of the method is a forward model for computing the cross-correlation $C(\mathbf{x}_\alpha, \mathbf{x}_\beta)$ between any pair of receivers α and β:

$$C(\mathbf{x}_\alpha, \mathbf{x}_\beta; \omega) = P(\omega) \int d^2\mathbf{x}\; G^*(\mathbf{x}_\alpha, \mathbf{x}; \omega) G(\mathbf{x}_\beta, \mathbf{x}; \omega) \sigma(\mathbf{x}), \tag{1}$$

where ω is angular frequency, P is the source power spectrum, G is the Green function for the medium, σ is the source strength, and the position coordinate $\mathbf{x}$ is limited to a horizontal plane (approximating an area on the Earth's surface). The asterisk denotes complex conjugation. This follows from the formulation of Tromp et al. (2010), subject to the following assumptions (e.g. Malkoti et al. 2021; Xu et al. 2019):

(i) all ambient seismic sources are confined to the Earth's surface, so that the integral in (1) is a surface integral

(ii) all sources have the same spectral shape $P(\omega)$, so that the power spectral density (S) of noise sources can be separated into its positional and frequency contributions, i.e. $P(\omega)\sigma(\mathbf{x}) = S(\mathbf{x}, \omega)$.

The frequency-domain expression (1) can be evaluated semi-analytically when closed form solutions for G are available — such as in a homogeneous (Datta et al. 2019) or 1-D (Malkoti et al. 2021) medium.

In anticipation of numerically solving the wave equation for heterogeneous media, we recast the expression for crosscorrelation in equation (1) in terms of the wavefields u:

$$C(\mathbf{x}_\alpha, \mathbf{x}_\beta; \omega) = \int d^2\mathbf{x}\; u^*(\mathbf{x}, \mathbf{x}_\alpha; \omega) u(\mathbf{x}, \mathbf{x}_\beta; \omega) \sigma(\mathbf{x}), \tag{2}$$

with $u(\mathbf{x}, \mathbf{x}_\alpha; \omega) = P(\omega)^{1/2} G(\mathbf{x}, \mathbf{x}_\alpha; \omega)$. Note that source-receiver reciprocity has also been invoked for computational efficiency, turning every receiver location into a source (e.g. Hanasoge 2014; Xu et al. 2019). The monochromatic wavefields in equation (2) can be computed in the frequency domain (e.g. Kumar et al. 2022). However, we use a time-domain finite difference solver implemented using the "Devito" package (Louboutin et al. 2019; Luporini et al. 2020). The uniform finite-difference stencil is second-order in time and fourth-order in space. Equation (2) in the time domain is

$$C(\mathbf{x}_\alpha, \mathbf{x}_\beta; t) = \int d^2\mathbf{x} \int_{-\infty}^{\infty} d\tau\; u(\mathbf{x}, \mathbf{x}_\alpha; \tau) u(\mathbf{x}, \mathbf{x}_\beta; t + \tau)\, \sigma(\mathbf{x}). \tag{3}$$

We obtain $u(\mathbf{x}, \mathbf{x}_\alpha; \tau)$ as the solution to the acoustic wave equation with a source wavelet equal to the inverse Fourier transform of $P(\omega)^{1/2}$. Provided that the computed wavefields $u(\mathbf{x}, \mathbf{x}_\alpha)$ can be stored in memory, N numerical simulations are required to obtain all possible cross-correlations for an N-receiver array. In the inverse problem of estimating $\sigma(\mathbf{x})$, these N simulations, once performed at the start, are not required to be repeated every iteration, because the velocity model is held fixed.

2.2 Model parameterization

As in Datta et al. (2019), the model space is parameterized using a set of 2-D Gaussian basis functions, $B_j(\mathbf{x})$. In this study, we introduce a non-negative parameterization to ensure that the iterative optimization scheme (Section 2.3) does not lead to unphysical, negative values for $\sigma(\mathbf{x})$:

$$\sigma(\mathbf{x}) = \sum_j m_j^2 B_j(\mathbf{x}), \tag{4}$$

m_j being the basis function coefficients that are directly inverted for. We note that alternate means of enforcing positivity are available, such as in Xu et al. (2019). A second feature of our parameterization is that the basis functions are present uniformly throughout the domain, rather than merely in a ring surrounding the receiver array (Datta et al. 2019). The size and spacing of the Gaussian basis are user-controlled parameters, held fixed during inversion. The specifications used to obtain the results presented in this paper, are listed in Table 3.1.

2.3 Inversion Strategy

We follow the inversion strategy detailed in Datta et al. (2019, Appendix A), subject to minor changes necessitated by the model parameterization, equation (4). To summarize, we use a misfit function defined by Hanasoge (2013):

$$\chi = \frac{1}{2}\sum_i \left(\ln \frac{E_i^{obs}}{E_i^{syn}}\right)^2, \tag{5}$$

where the index i runs over receiver pair combinations, and E, the measurement, is the waveform energy in a time window of interest $w(t)$:

$$E_i = \sqrt{\int w(t) C_i^2(t) dt} \tag{6}$$

For inversion of noise-free synthetic data, as done in this study, we use a window spanning the entire positive or negative correlation branch.

Local optimization techniques require the gradient of χ, or a misfit kernel K satisfying $\delta\chi = -\int K(\mathbf{x})\delta\sigma(\mathbf{x})d^2\mathbf{x}$. This misfit kernel is the sum of individual source kernels for each receiver pair (K_i), weighted by the corresponding misfit (Hanasoge 2013):

$$K = \sum_i \ln\left(\frac{E_i^{obs}}{E_i^{\mathrm{syn}}}\right) K_i(\mathbf{x}) \tag{7}$$

Using (4), we get the following expression for the gradient ($\mathbf{g}$) of χ:

$$g_j = \frac{\partial \chi}{\partial m_j} = -\int 2K(\mathbf{x}) m_j B_j(\mathbf{x})\; d^2\mathbf{x} \tag{8}$$

K, and therefore g, can be obtained by either evaluating (7), which requires all the individual source kernels K_i, or by adjoint techniques, which build K from adjoint wavefields and 'event kernels' (Tromp et al. 2010), without access to the individual K_i. We use the former, non-adjoint approach. Using an analogy from earthquake traveltime tomography, this is akin to the difference between calculating individual banana doughnut kernels (e.g. Dahlen et al. 2000) or not (Tromp et al. 2005).

Our approach remains computationally feasible because numerical simulations are not required to obtain the K_i in every iteration, as explained in Section 2.1. Furthermore, we parallelise the implementation over the individual receivers. The advantage of this inversion strategy is that in addition to the gradient, it gives us access to the Jacobian through the individual kernels. Combining (7) and (8), the elements of our Jacobian matrix ($\mathbf{J}$) are:

$$J_{ij} = \int 2K_i(\mathbf{x}) m_j B_j(\mathbf{x})\, d^2\mathbf{x} \tag{9}$$

The Jacobian can in turn be used to build an approximation to the Hessian operator, and optimization methods such as the Gauss-Newton method, can be employed. For details of how this is done, and complete derivations of equations (8) and (9), the reader is referred to Appendix A of Datta et al. (2019).

3 SYNTHETIC TESTS

We conduct a series of synthetic tests using the field array geometry of Datta et al. (2019), which corresponded to an exploration seismic deployment by Shell. This choice is motivated by the relatively large number of receivers (289) in the array, which allows us to explore the effects of different array sizes and path densities, by randomly picking different subsets of receivers. We present results in this paper for two sub-array geometries, one with 20 and the other with 50 receivers (Figure 1, parts b and c, respectively). Synthetic tests with more than 50 receivers did not produce significantly different results.

Our modelling domain for all tests is 50 km $\times$ 50 km, and other simulation parameters are listed in Table 3.1. These specific choices result in source distributions represented by a total of

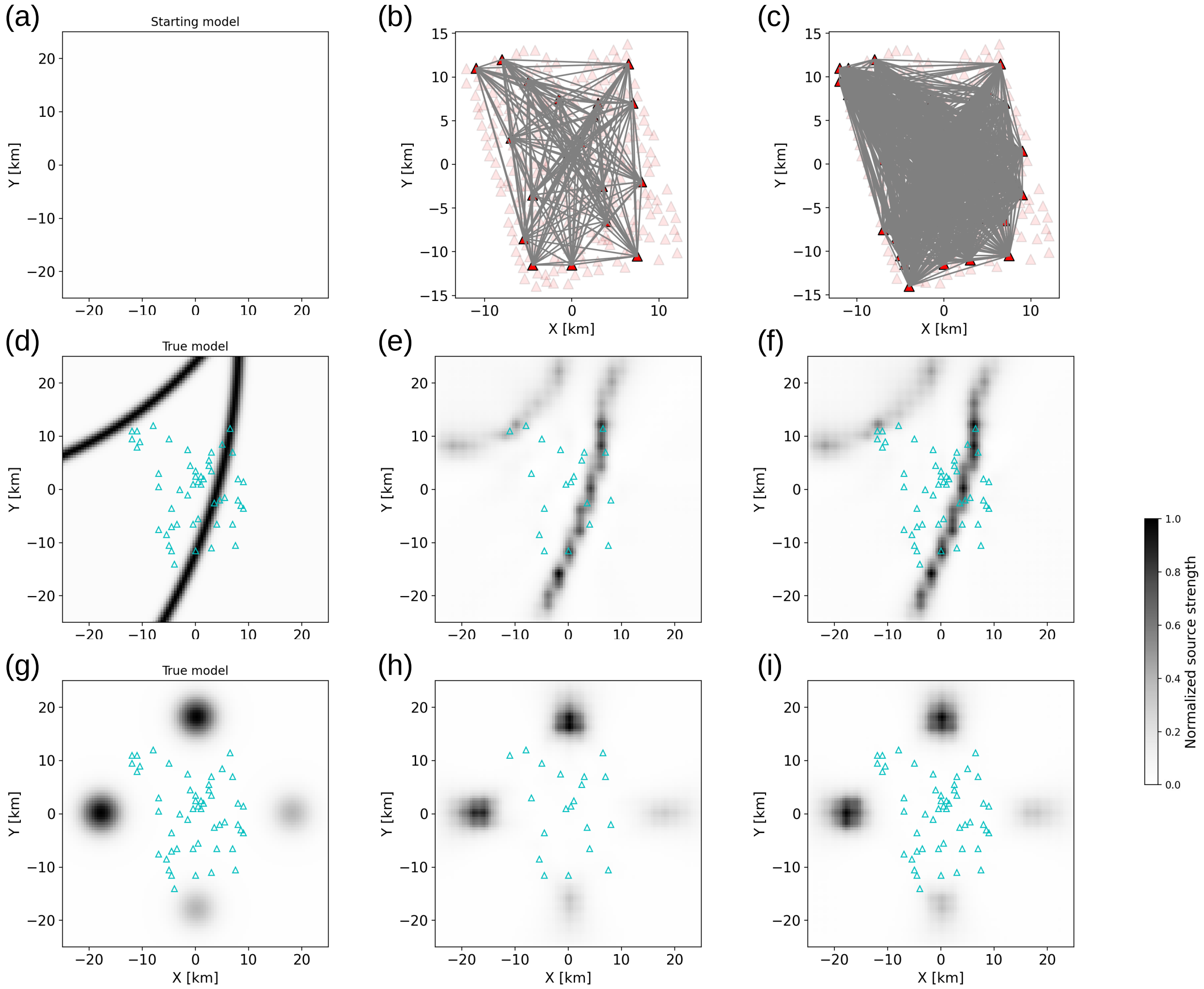

Figure 1. Source inversion results with homogeneous velocity models. (a) Starting model for all inversions. (b)-(c) Tomographic setup used for inversion: map with 20 and 50 receivers selected respectively (red triangles), along with inter-receiver ray paths (grey lines). (d) TSM-1, shown with the 50 receivers selected in (c). (e)-(f) Inversion results for TSM-1, using 20 and 50 receivers respectively. (g) TSM-2, shown with the 50 receivers selected in (c). (h)-(i) Inversion results for TSM-2, using 20 and 50 receivers respectively. All source distributions are shown normalized by their maximum value (to focus on relative source strength), with the exception of the starting model (a), which is normalized with respect to the test models to illustrate its low amplitude.

625 basis functions. We present results for two test source models, TSM-1 (Fig. 1d) and TSM-2 (Fig. 1g). In actual field scenarios, TSM-1 may represent, for example, roads situated close to or passing through, the receiver array. TSM-2 is more of a toy model, containing sources of varying strengths located entirely outside the array. The test models are built independently, without using the parameterization (4), which is reserved for the inverse problem.

For both test models, we generate noise-free synthetic data to serve as "observed data". A uniform source distribution (Figure 1a) is used as a prior as well as the initial model for inversion. This initial model has very low amplitude compared to the test models, but it cannot be zero because of the logarithmic misfit function (5) used in the inversion.

Figure 1 shows that the inversion recovers true source locations and shapes fairly well, for both test models. As expected, results with 50 receivers are better than those with 20, but the improvement is modest, especially for sources lying outside the receiver array (TSM-2). The pixellated appearance of the inversion results as compared to the test models, is due to the parameterization (4) and the size of basis functions used (Table 3.1). Finally, we note that either analytical or numerical modelling may be used in these inversions, because a homogeneous medium is assumed. For consistency with the rest of the paper, we have presented results obtained with numerical modelling. The results with analytical Green functions were similar to those in Figure 1 and have not been shown.

3.1 Impact of heterogeneous velocity structure

To investigate the effects of heterogeneous structure, we use two types of velocity models to generate the test data: a single low velocity anomaly (Figure 2) and a checkerboard (Figure 3). In both cases we consider perturbation amplitudes of 5, 10 and 20% relative to the reference velocity of 2 km/s (used in Fig. 1). Inversions are then performed both with and without accurate velocity models. In this section, we present tests performed with the 50-receiver array geometry only.

When the velocity information provided in inversion is accurate, we obtain results that are all nearly identical to the homogeneous velocity case (Fig. 2). The inverse modelling can tolerate errors in velocity information up to 10%, but artefacts appear for the case of 20% velocity heterogeneity. Also, sources outside the array are not retrieved accurately in this case. With the checkerboard velocity model, inversion artefacts are less pronounced (Figure 3), but the sources outside the array are very faintly recovered for a magnitude of 20% heterogeneity. Similar tests with the second source model, TSM-2, are presented in Appendix A. In contrast to TSM-1, TSM-2 is a simpler model and the sources exist only outside the array. The stronger sources to the North

Parameter	Value
Uniform grid spacing	0.5 km
Basis function width	5 km
Basis function spacing	2 km
Reference wavespeed	2 km/s
Time series length	50 s
Central frequency	0.2 Hz

Table 1. Simulation parameters used.

and West of the array have been recovered for both the Gaussian anomaly (Figure A1) and the checkerboard model (Figure A2). The weaker sources (to the East and South) are not recovered well in both the instances, particularly for the case of 20% velocity heterogeneity.

It should be emphasised that the $\sigma(\mathbf{x})$ starting model is the same (see Fig. 1a) for all tests in this section and in Appendix A,. On the other hand, the optimal value of the damping parameter used in inversion (Datta et al. 2019, Appendix A), is determined separately in each case by independent L-curve analysis (Hansen & O'Leary 1993).

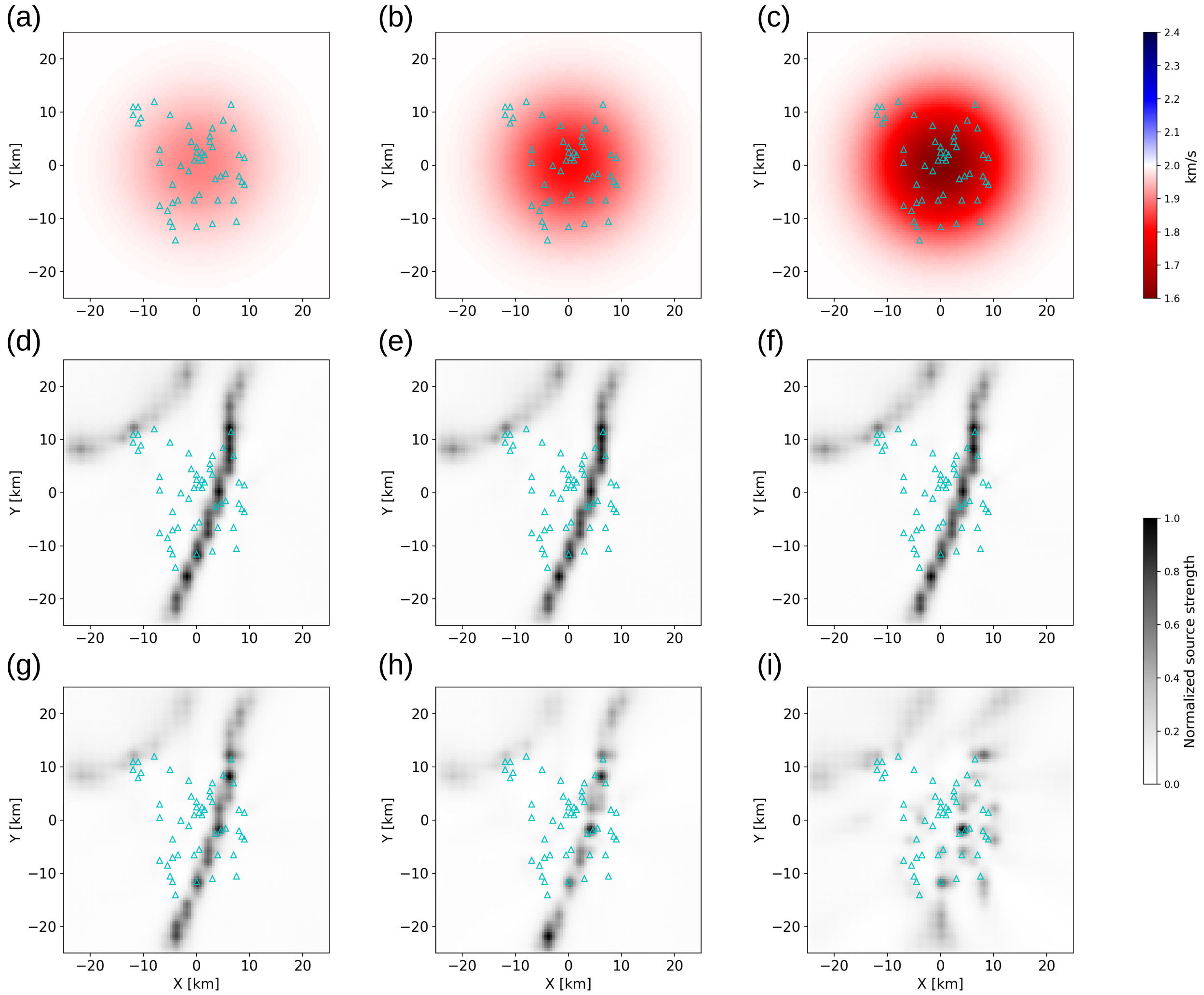

Figure 2. Source inversion results with 2-D velocity models. Top row: Velocity models with a perturbation amplitude of (a) 5% (b) 10% (c) 20%. Middle row: Inversion results for TSM 1, obtained using an accurate velocity model, i.e. velocity models (a)-(c) are used to generate synthetic test data, as well as in source inversion leading to the corresponding results (d)-(f). Bottom row: Results of inversion performed without an accurate velocity model, i.e. velocity models (a)-(c) are used to generate synthetic test data, but source inversion is performed using a homogeneous velocity model. In all cases, the starting (source) model for inversion is the same as in Figure 1a.

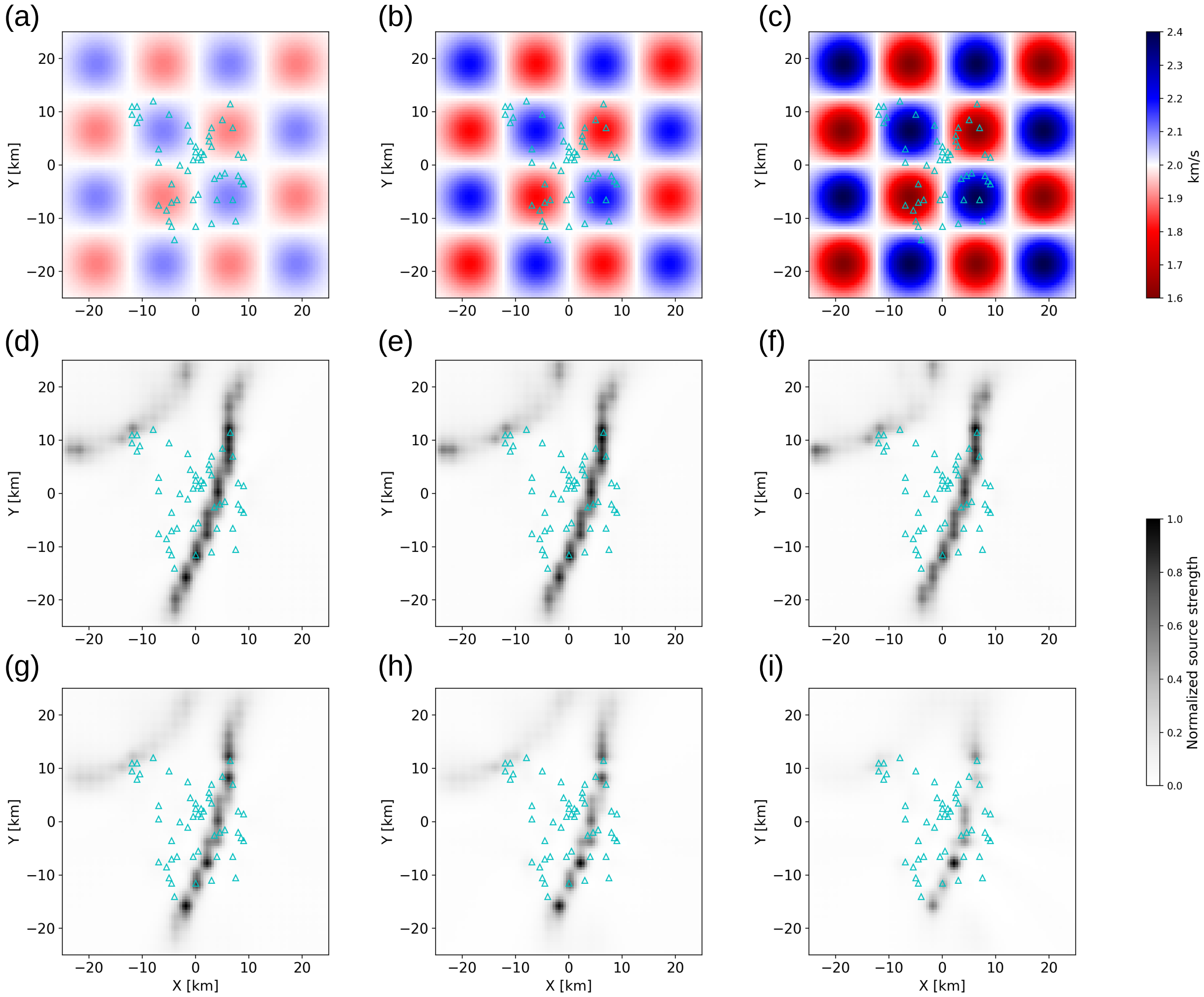

Figure 3. Similar to Figure 2, but using checkerboard-style velocity models.

4 CONCLUSIONS

Our synthetic tests have shown that:

(i) the inversion technique presented in this paper is able to recover source distributions anywhere in the modelling domain, under ideal conditions of error-free modelling.

(ii) accurate modelling of velocity structure, within the acoustic approximation, has limited impact on ambient noise source inversion. Detrimental effects of assuming a simplistic velocity model are seen only when the assumed model is a very poor approximation to the true structure. For media with weak lateral heterogeneity, even the simplest approximation of a homogeneous medium (with a reference wavespeed accurate to within 10%) is acceptable. It becomes unacceptable when true wavespeed variations exceed 20% of the assumed reference value.

The second point above is relevant for realistic scenarios where the velocity structure is not known *a priori*. With real data, one can expect unmodelled lateral heterogeneity to have a greater impact on source inversion, because real data would likely contain noise as well as 'modelling error' (both of which were absent in the synthetic data of Section 3).

5 DISCUSSION

We have introduced an acoustic full waveform inversion technique for ambient noise source distribution. Although more sophisticated techniques, which account for Earth's three-dimensional, elastic (and anelastic) structure already exist (e.g. Ermert et al. 2017, 2021), our method occupies a niche within the field. Compared to 3-D elastic FWI, it incorporates a significant amount of modelling rigour, at a fraction of the computational cost — all simulations presented in this paper were performed on a desktop computer. Further, it affords an opportunity to leverage results from the immensely popular field of ray-based ambient noise tomography. Surface wave group velocity maps produced by ray-based methods (e.g. Shekar et al. 2022) can be used to characterize Earth structure in our source inversion scheme. More generally, such maps can be used as starting structure models in a future joint source-structure acoustic inversion scheme, which may serve to refine traditional ambient noise tomographic models. The obvious limitation of our technique is the acoustic regime, which limits us to membrane wave simulations and precludes the use of any multicomponent information from ambient noise cross-correlations (e.g. Xu & Mikesell 2017; Malkoti et al. 2021).

In this paper, we have used the developed technique to investigate the impact of velocity heterogeneity on ambient noise source inversion. We also used it to demonstrate recovery of noise sources located outside the receiver array, an important capability of small-aperture arrays deployed for local-scale investigations. We surmise that the reason for our success is our Hessian-based optimization scheme, as opposed to just gradient-based optimization. Indeed, the inverse of the approximate Hessian can act as a focusing operator that compensates for uneven illumination and finite bandwidth of the wavefields (Pratt et al. 1998). However, we note that the Gauss-Newton approach is only feasible for small aperture arrays used in local- to (small) regional- scale studies.

Application of our technique to real data is a subject of ongoing research. In the future, its technical scope can be widened in several ways. For example, the assumption of uniform spectral character of all ambient sources can be relaxed to invert for space- as well as frequency- dependent ambient source distribution (e.g. Ermert et al. 2017, 2021). While this considerably expands the parameter space, techniques like sparsity promotion (e.g. Shekar & Sethi 2019) can be employed to constrain the inversion. Another line of development would be to extend to 3-D elastic modelling, and we note that this is possible with the "Devito" package itself.

ACKNOWLEDGEMENTS

This research is supported by the Department of Science and Technology, Government of India, via an INSPIRE Faculty grant to AD. PLK gratefully acknowledges support from this grant while at IISER Pune.

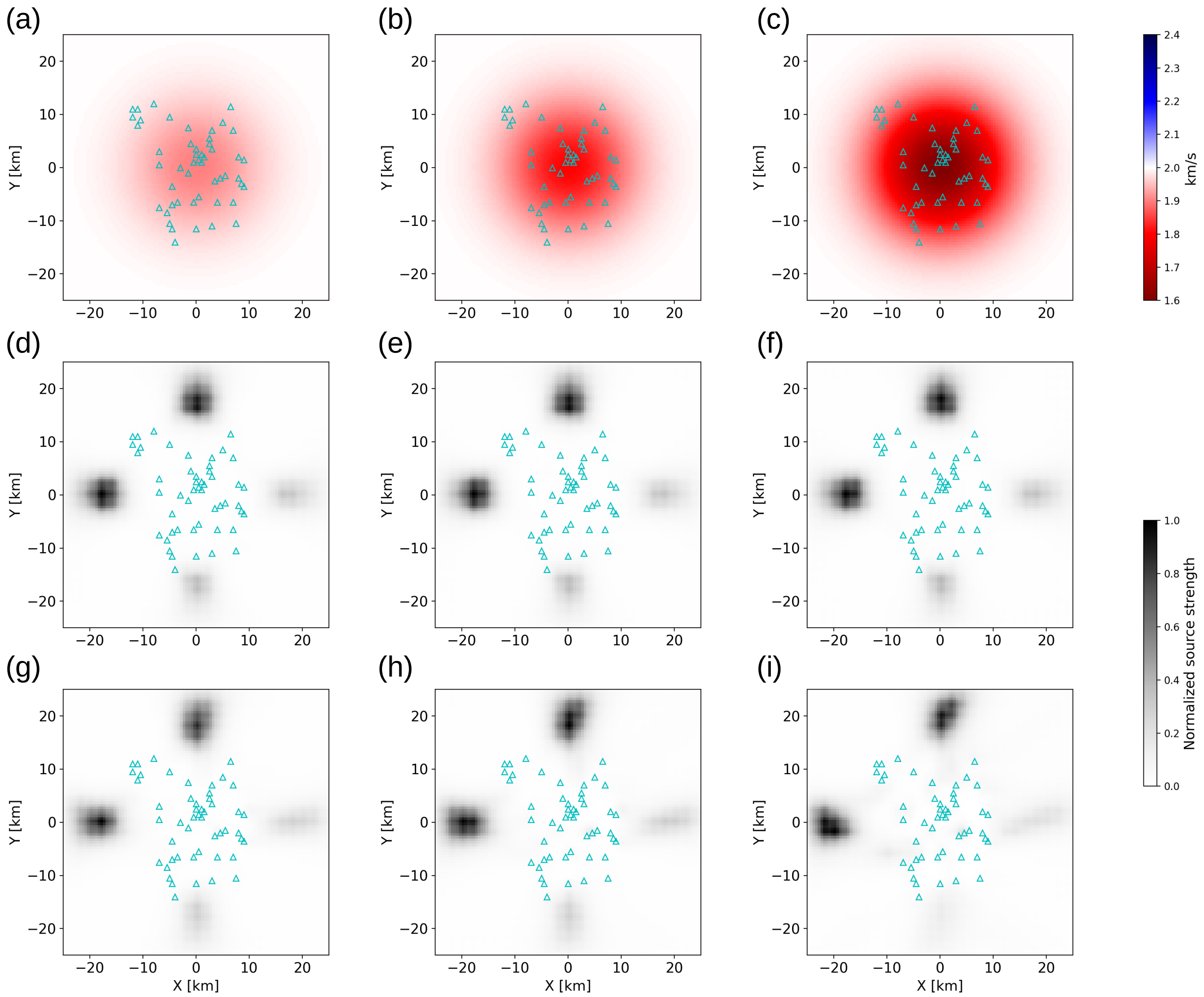

Figure A1. Similar to Figure 2 in the main text but for TSM-2.

APPENDIX A: SYNTHETIC TESTS FOR TSM-2

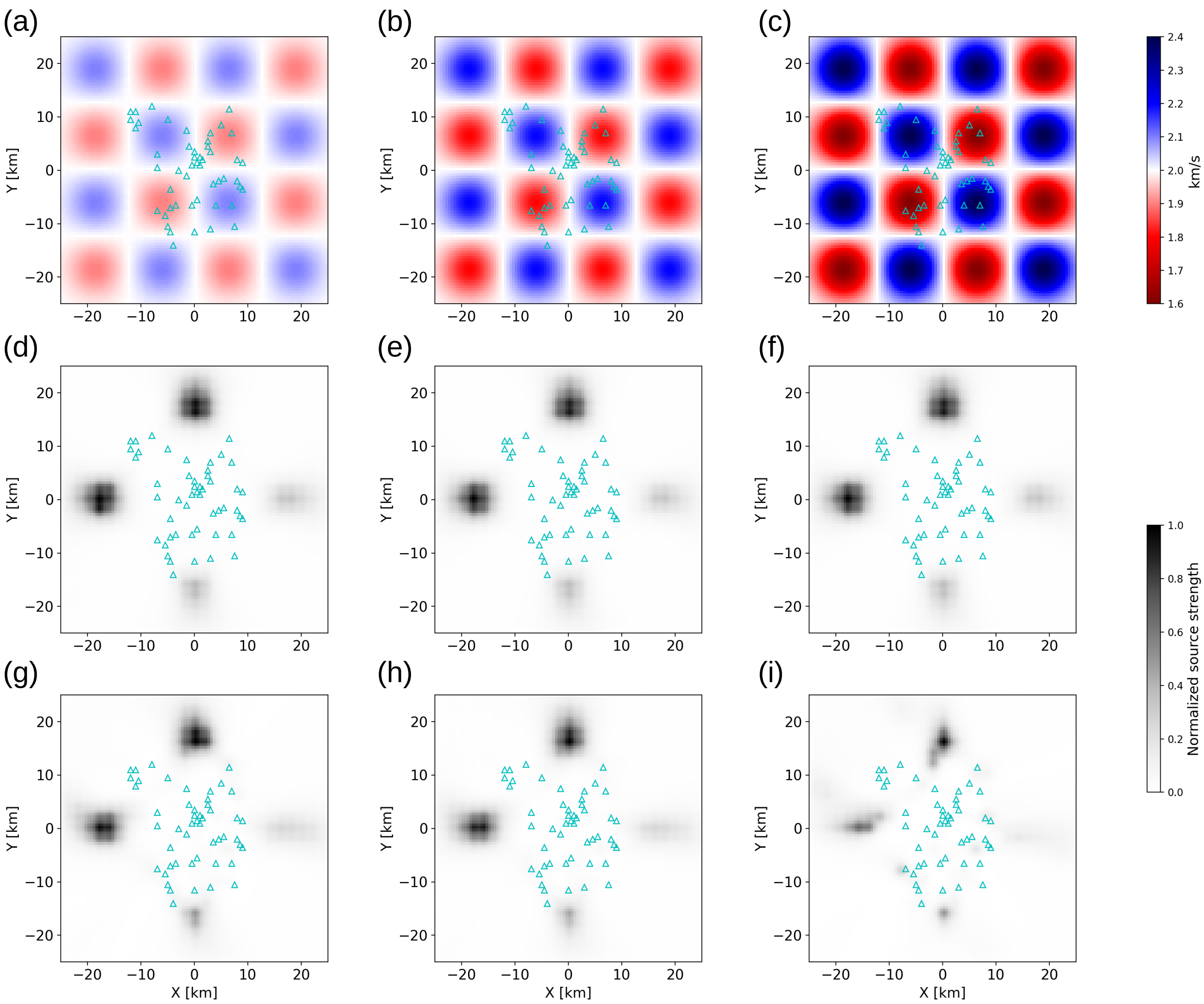

Figure A2. Similar to Figure 3 in the main text but for TSM-2.

DATA AVAILABILITY

No new data were generated or analysed in support of this research. The source inversion code used in this work will be made available on github: https://github.com/ arjundatta23/cc_kern_inv.

REFERENCES

Aso, N., Tsai, V. C., Schoof, C., Flowers, G. E., Whiteford, A., & Rada, C., 2017. Seismologically observed spatiotemporal drainage activity at moulins, *Journal of Geophysical Research: Solid Earth*, **122**, 9095–9108.

Bensen, G. D., Ritzwoller, M. H., Barmin, M. P., Levshin, A. L., Lin, F., Moschetti, M. P., Shapiro, N. M., & Yang, Y., 2007. Processing seismic ambient noise data to obtain reliable broad-band surface wave dispersion measurements, *Geophysical Journal International*, **169**, 1239–1260.

Cros, E., Roux, P., Vandemeulebrouck, J., & Kedar, S., 2011. Locating hydrothermal acoustic sources at old faithful geyser using matched field processing, *Geophysical Journal International*, **187**, 385–393.

Dahlen, F. A., Hung, S.-H., & Nolet, G., 2000. Fréchet kernels for finite-frequency traveltimes-i. theory, *Geophysical Journal International*, **141**, 157–174.

Datta, A., Hanasoge, S., & Goudswaard, J., 2019. Finite frequency inversion of cross-correlation amplitudes for ambient noise source directivity estimation, *Journal of Geophysical Research: Solid Earth*, **124**, 6653–6665.

Ermert, L., Villaseñor, A., & Fichtner, A., 2016. Cross-correlation imaging of ambient noise sources, *Geophysical Journal International*, **204**, 347–364.

Ermert, L., Sager, K., Afanasiev, M., Boehm, C., & Fichtner, A., 2017. Ambient seismic source inversion in a heterogeneous earth: Theory and application to the earth's hum, *Journal of Geophysical Research: Solid Earth*, **122**, 9184–9207.

Ermert, L. A., Sager, K., Nissen-Meyer, T., & Fichtner, A., 2021. Multifrequency inversion of global ambient seismic sources, *Geophysical Journal International*, **225**, 1616–1623.

Fichtner, A., 2014. Source and processing effects on noise correlations, *Geophysical Journal International*, **197**, 1527–1531.

Fichtner, A., Stehly, L., Ermert, L., & Boehm, C., 2017. Generalized interferometry – i: theory for interstation correlations, *Geophysical Journal International*, **208**, 603–638.

Gal, M., Reading, A. M., Ellingsen, S. P., Gualtieri, L., Koper, K. D., Burlacu, R., Tkalčiïc, H., & Hemer, M. A., 2015. The frequency dependence and locations of short-period microseisms generated in the southern ocean and west pacific, *Journal of Geophysical Research: Solid Earth*, **120**, 5764–5781.

Gerstoft, P. & Tanimoto, T., 2007. A year of microseisms in southern california, *Geophysical Research Letters*, **34**, L20304.

Hanasoge, S. M., 2013. The influence of noise sources on cross-correlation amplitudes, *Geophysical Journal International*, **192**, 295–309.

Hanasoge, S. M., 2014. Measurements and kernels for source-structure inversions in noise tomography, *Geophysical Journal International Geophys. J. Int*, **196**, 971–985.

Hansen, P. C. & O'Leary, D. P., 1993. The use of the l-curve in the regularization of discrete ill-posed problems, *Siam Journal on Scientific Computing*, **14**, 1487–1503.

Igel, J. K., Ermert, L. A., & Fichtner, A., 2021. Rapid finite-frequency microseismic noise source inversion at regional to global scales, *Geophysical Journal International*, **227**, 169–183.

Juretzek, C. & Hadziioannou, C., 2016. Where do ocean microseisms come from? a study of love-to-rayleigh wave ratios, *Journal of Geophysical Research: Solid Earth*, **121**, 6741–6756.

Kimman, W. P. & Trampert, J., 2010. Approximations in seismic interferometry and their effects on surface waves, *Geophysical Journal International*, **182**, 461–476.

Kumar, N., Shekar, B., & Singh, S., 2022. A nodal integral scheme for acoustic wavefield simulation, *Pure and Applied Geophysics*, **179**, 3677–3691.

Labedz, C. R., Bartholomaus, T. C., Amundson, J. M., Gimbert, F., Karplus, M. S., Tsai, V. C., & Veitch, S. A., 2022. Seismic mapping of subglacial hydrology reveals previously undetected pressurization event, *Journal of Geophysical Research: Earth Surface*, p. e2021JF006406.

Liu, Q., Koper, K. D., Burlacu, R., Ni, S., Wang, F., Zou, C., Wei, Y., Gal, M., & Reading, A. M., 2016. Source locations of teleseismic p, sv, and sh waves observed in microseisms recorded by a large aperture seismic array in china, *Earth and Planetary Science Letters*.

Louboutin, M., Lange, M., Luporini, F., Kukreja, N., Witte, P. A., Herrmann, F. J., Velesko, P., & Gorman, G. J., 2019. Devito (v3.1.0): an embedded domain-specific language for finite differences and geophysical exploration, *Geoscientific Model Development*, **12**(3), 1165–1187.

Luporini, F., Louboutin, M., Lange, M., Kukreja, N., Witte, P., Hückelheim, J., Yount, C., Kelly, P. H. J., Herrmann, F. J., & Gorman, G. J., 2020. Architecture and performance of devito, a system for automated stencil computation, *ACM Trans. Math. Softw.*, **46**(1).

Malkoti, A., Datta, A., & Hanasoge, S. M., 2021. Rayleigh-wave h/v ratio measurement from ambient noise cross-correlations and its sensitivity to vp: a numerical study, *Geophysical Journal International*, **227**, 472–482.

Pratt, R. G., Shin, C., & Hick, G. J., 1998. Gauss–newton and full newton methods in frequency–space seismic waveform inversion, *Geophys. J. Int.*, **133**, 341–362.

Retailleau, L. & Gualtieri, L., 2019. Toward high-resolution period-dependent seismic monitoring of tropical cyclones, *Geophysical Research Letters*, **46**, 1329–1337.

Roux, P., Sabra, K. G., Kuperman, W. A., & Roux, A., 2005. Ambient noise cross correlation in free space: Theoretical approach, *The Journal of the Acoustical Society of America*, **117**, 79–84.

Sager, K., Boehm, C., Ermert, L., Krischer, L., & Fichtner, A., 2018a. Sensitivity of seismic noise correlation functions to global noise sources, *Journal of Geophysical Research: Solid Earth*.

Sager, K., Ermert, L., Boehm, C., & Fichtner, A., 2018b. Towards full waveform ambient noise inversion, *Geophysical Journal International*, **212**, 566–590.

Sager, K., Boehm, C., Ermert, L., Krischer, L., & Fichtner, A., 2020. Global-scale full-waveform ambient noise inversion, *Journal of Geophysical Research: Solid Earth*, **125**, e2019JB018644.

Shapiro, N. M., 2019. Applications with surface waves extracted from ambient seismic noise, in *Seismic Ambient Noise*, pp. 218–238, eds Nakata, N., Gualtieri, L., & Fichtner, A., Cambridge Univ. Press.

Shapiro, N. M. & Campillo, M., 2004. Emergence of broadband rayleigh waves from correlations of the ambient seismic noise, *Geophysical Research Letters*, **31**, n/a–n/a.

Shekar, B. & Sethi, H. S., 2019. Full-waveform inversion for microseismic events using sparsity constraints, *Geophysics*, **84**(2), KS1–KS12.

Shekar, B., Mohan, G., & Singh, S. K., 2022. Structural information derived from ambient noise tomography over a hydrocarbon producing region in cachar fold belt, lower assam, northeast india, *Geophysical Prospecting*, **n/a**(n/a).

Snieder, R., 2004. Extracting the green's function from the correlation of coda waves: A derivation based on stationary phase, *Physical Review E*, **69**, 046610.

Tian, Y. & Ritzwoller, M. H., 2015. Directionality of ambient noise on the juan de fuca plate: implications for source locations of the primary and secondary microseisms, *Geophysical Journal International*, **201**, 429–443.

Tromp, J., Tape, C., & Liu, Q., 2005. Seismic tomography, adjoint methods, time reversal and banana-doughnut kernels, *Geophysical Journal International*, **160**, 195–216.

Tromp, J., Luo, Y., Hanasoge, S., & Peter, D., 2010. Noise cross-correlation sensitivity kernels, *Geophysical Journal International*, **183**, 791–819.

Tsai, V. C., Minchew, B., Lamb, M. P., & Ampuero, J. P., 2012. A physical model for seismic noise generation from sediment transport in rivers, *Geophysical Research Letters*, **39**, 2404.

Xu, Z. & Mikesell, T. D., 2017. On the reliability of direct rayleigh-wave estimation from multicomponent cross-correlations, *Geophysical Journal International*, **210**, 1388–1393.

Xu, Z., Mikesell, T. D., Gribler, G., & Mordret, A., 2019. Rayleigh-wave multicomponent cross-correlation-based source strength distribution inversion. part 1: Theory and numerical examples, *Geophysical Journal International*, **218**, 1761–1780.

Xu, Z., Mikesell, T. D., Umlauft, J., & Gribler, G., 2020. Rayleigh-wave multicomponent crosscorrelation-based source strength distribution inversions. part 2: a workflow for field seismic data, *Geophysical Journal International*, **222**, 2084–2101.

Yao, H. & van der Hilst, R. D., 2009. Analysis of ambient noise energy distribution and phase velocity bias in ambient noise tomography, with application to se tibet, *Geophysical Journal International*, **179**, 1113–1132.

Zhou, C., Xia, J., Cheng, F., Pang, J., Chen, X., Xing, H., & Chang, X., 2022. Passive surface-wave waveform inversion for source-velocity joint imaging, *Surveys in Geophysics*, **43**, 853–881.